Shear-induced permeability anisotropy in liquefiable sands

José Salomón[1#], *Fernando* Patino-Ramirez[1], and *Catherine* O'Sullivan[1]

Dept. Of Civil and Environmental Engineering, Imperial College London, South Kensington, London, SW7 2AZ, UK

[#]*Corresponding author: jose.salomon19@imperial.ac.uk*

ABSTRACT

In principle, numerical simulations of boundary value problems that involve fluid-soil interaction should account for the evolution of permeability due to soil deformation. For many applications of interest in geotechnical engineering, an accurate assessment of the permeability is key to an accurate prediction of settlements and pore water pressure changes. Finite element models rely on laboratory or field testing to characterise permeability; however, these methods cannot easily evaluate anisotropy or moderate variations of permeability. Current testing tools have a limited accuracy and a rigid experimental set-up, and are usually restricted to consider one flow direction. In this study, the influence of shearing on the intrinsic permeability and the anisotropy of permeability in medium-loose liquefiable sands is investigated. The discrete element method (DEM) was used to simulate monotonic undrained and drained triaxial test simulations on model soils comprising spherical particles. The particle positions were recorded at discrete strain levels and the data were taken as input into finite volume method (FVM) simulations which were used to evaluate intrinsic permeability in selected sub-samples. In the FVM simulations, permeability was evaluated in the three orthogonal directions. The results indicate that shear deformation induces an anisotropy in permeability, in both drained and undrained triaxial conditions and this anisotropy increases with axial strain. Specifically, the results show an increase in permeability in the direction of the major principal stress, whereas a reduction permeability is observed in the orthogonal plane. Undrained simulations exhibit a jump in vertical permeability around the liquefaction onset; this can be attributed to the sudden loss of particle contacts.

Keywords: permeability anisotropy; discrete element method; finite volume method; shearing.

1. Introduction

Continuum numerical models of soil-fluid interaction must account for permeability changes in the soil mass. In two-way Finite Element Method (FEM) coupling, changes in pore water pressure are determined by continuity conditions and Darcy's law, which strongly depends on the soil permeability. In many continuum frameworks the permeability is updated when the state of the system varies (e.g. in terms of effective stresses or volumetric changes). Complex phenomena as embankment deformation in liquefiable soils and sand boil ejecta have been successfully reproduced using this type of coupling scheme (Elgamal et al. 2002, Dinesh et al. 2022, Hutabarat & Bray 2022). In both scenarios, the evolution of permeability has a major role in predicting settlements and pore water pressure changes (Sahir et al. 2014, Malekmakan et al. 2021, Hutabarat & Bray, 2022).

Analysts developing the input for FEM simulations usually rely on permeameter or in-situ tests to characterize permeability. However, due to inherent limitations on the procedures and devices, and the variability of in-situ correlations, moderate changes in permeability can hardly be captured (Chapuis 2012, Robertson 2010). According to Duncan (2000), a coefficient of variation of 68-90% is expected for saturated permeability measurements. Elements such as the type of wall (i.e. flexible or rigid) adopted in the permeameter or the type of porous stone can bias laboratory values up to one or two orders of magnitude (Daniel et al. 1985, Bayoumi et al. 2022, Shaker et al. 2022).

The variation in permeability due to changes in effective confining pressure can be evaluated through permeameter tests in a triaxial cell (ASTM 2016). More general stress states can also be explored using centrifuge or shaking table tests (Adamidis & Madabushi 2018, Xie et al. 2021, Fioravante et al. 2021). While these methods can be adapted to represent a variety of boundary value problems and stress states, current approaches cannot assess permeability in multiple directions. The effect of permeability anisotropy in the behaviour of embedded piles and offshore foundations has been numerically evaluated by Wang (2021), and Li et al. (2018). Simulations indicate that permeability anisotropy affects the dissipation time and the magnitude of the pore water pressure.

Efforts to assess permeability variations and anisotropy during shearing were made by Kuhn et al. (2016). The evolution of permeability in dense dilative sands under biaxial drained loading was investigated by means of the discrete element method (DEM) and lattice Boltzmann (LBM) simulations. Kuhn et al. (2016) concluded that permeability anisotropy is induced by shearing, and its magnitude is closely correlated to fabric and volumetric changes.

Hitherto no study has shown how permeability evolves during shearing in medium-loose, liquefiable, sand samples. Researchers who have examined

experimental data have hypothesized that the measured permeability increases during liquefaction due to a loss of contact between particles (Haigh et al. 2012, Sahir et al. 2014).

In this study, the influence of shearing on intrinsic permeability and the anisotropy of permeability of liquefiable sands is investigated. For this purpose, DEM monotonic undrained and drained triaxial test simulations are carried out and characteristic strain levels are chosen. For each one of these strain levels, permeability is evaluated in three orthogonal directions by performing finite volume simulations of selected sub-samples.

2. DEM Simulations

2.1. Methodology

DEM samples were generated by randomly placing 20,172 spherical particles inside a cubical box. According to Huang et. al (2014), sample size effects can be neglected around this sample size. Radii were selected to resemble the particle size distribution (PSD) of Toyoura sand (Yang & Sze 2011), as shown in Fig. 1. Particle sizes and positions were used as input for the DEM simulations.

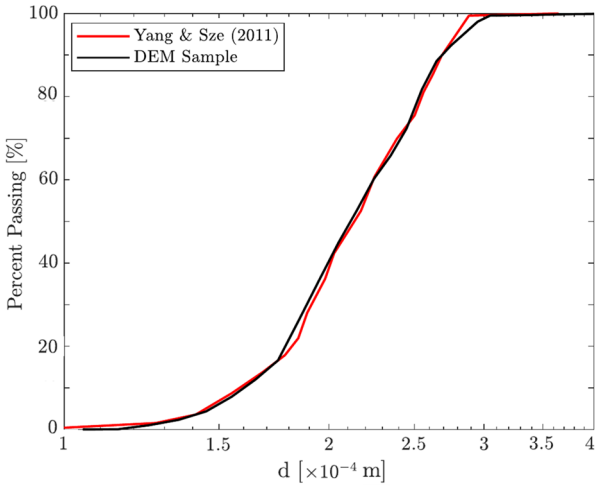

Figure 1. Particle size distribution. Comparison between Toyoura Sand (Yang & Sze, 2011) and DEM sample.

The DEM simulations were performed using the molecular dynamics open-source code LAMMPS (Plimpton, 1995). A simplified Hertz-Mindlin model was employed to calculate inter-particle normal and tangential forces as a function of particle overlap. Samples were isotropically compressed until an effective confining pressure of σ_c'=300kPa was attained. A loose to medium dense packing (e_0=0.631) was obtained by applying an interparticle friction coefficient of μ=0.13. All boundaries were considered periodic. A summary of the DEM simulation parameters is indicated in Table 1. Particle arrangement after the isotropic compression stage can be observed in Fig. 2.

During the shearing stage, the sample was compressed vertically with a constant strain rate of $\dot{\varepsilon}_z$ =0.17 1/s. Starting from the same initial isotropic stage (e_0=0.631), both drained and undrained shearing simulations were performed. In drained shearing, lateral boundaries were displaced so the effective confining pressure remained constant. Undrained condition was emulated by displacing the lateral boundaries to keep the volume of the sample constant. In both cases, an interparticle friction coefficient of μ=0.25 was employed (Huang et al. 2014). Samples were sheared to an axial strain of 10%. An inertial number of I_n=2.8x10^{-6} is estimated for the drained simulations, which is below the quasi-static limit of 10^{-4}-10^{-3}, usually assumed for these type of granular simulations (Shire et al., 2021).

Table 1. DEM simulation parameters.

Parameter	Value	Units
Shear modulus, G	29	GPa
Poisson's ratio, ν	0.12	-
Particle density, ρ_s	2670	kg/m^3
Interparticle friction, μ	0.13 (Isotropic compression) 0.25 (Shearing)	-
Timestep, Δt	5.37x10^{-9}	s
Local damping, η	0.1	-
Effective confining pressure, σ_c'	300	kPa

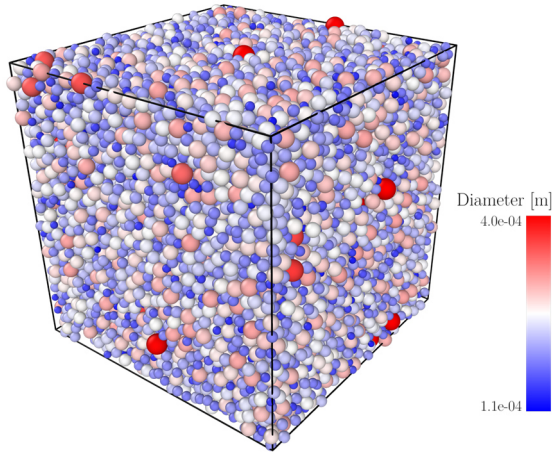

Figure 2. DEM sample. Toyoura Sand. Isotropic compression stage σ_c'=300kPa. e_0=0.631. 20,172 particles. The colorbar indicates particle diameter.

2.2. Shearing Stage Results

The overall sample responses during the two shear tests stage are shown in Fig. 3. The drained and undrained tests are represented in red and green lines, respectively. Fig. 3(a) displays the stress-strain curves in terms of the deviatoric stress, q, and the axial strain of the sample, ε_z. Likewise, Fig. 3(b) shows the variation of volumetric strain, ε_{vol} and excess pore water pressure, Δu as a function of the axial strain of the sample, ε_z. As a convention, compressive strains are considered positive.

A predominantly contractive behaviour is observed in both types of loading. In the drained sample, a maximum volumetric strain of 0.22% is attained at around 4% of axial strain. When the axial strain is beyond 8%, the response becomes dilative. A monotonic increase in the deviatoric stress throughout the loading phase can also be observed.

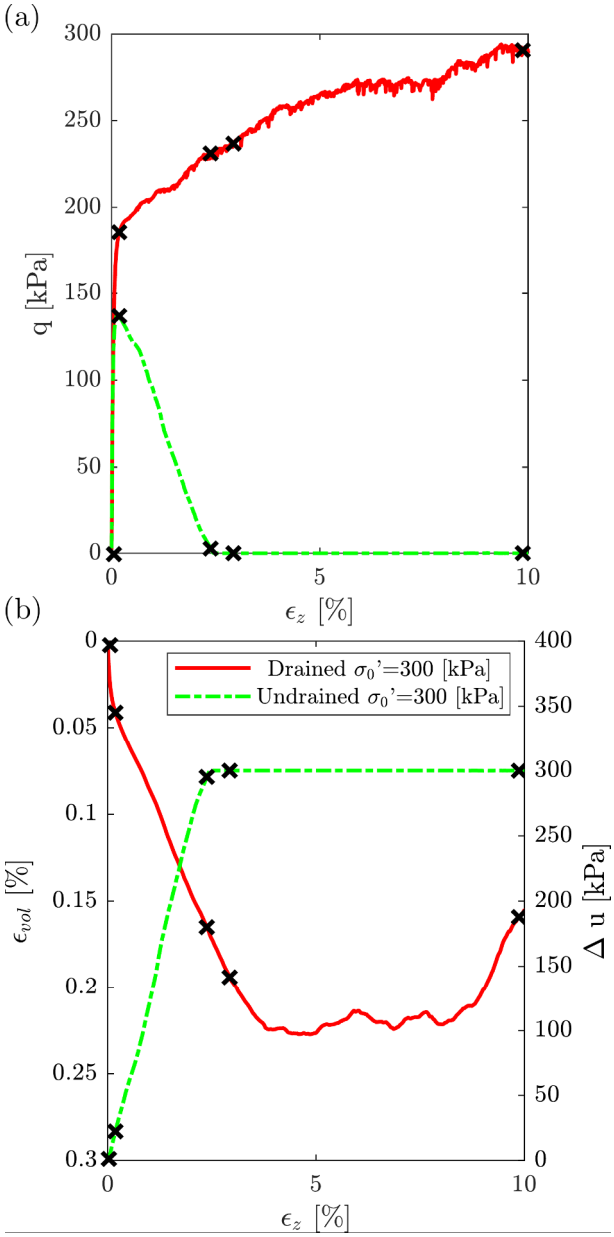

Figure 3. Triaxial drained and undrained test results. (a) axial strain versus deviatoric stress, (b) axial strain versus volumetric strain/pore water pressure. Black crosses indicate the strain levels selected for the finite-volume simulations.

The undrained test exhibits a peak at around 0.2% of axial strain followed by a reduction towards a fully liquefied state, where the effective confining pressure drops to zero. This condition persists for all subsequent strain levels. The observed behaviour is qualitatively consistent with triaxial data reported for Toyoura sand samples (Verdugo and Ishihara 1996, Yang & Sze 2011).

3. Permeability Tests

3.1. Methodology

From the DEM sheared samples, particle positions were extracted at five different strain levels. These levels were chosen to represent distinct features of undrained behaviour in loose sands (i.e. the isotropic state prior to shear deformation, peak stress, before liquefaction onset, after liquefaction onset, and liquefaction at further strains). The selected strain levels are depicted with black crosses in Fig. 3.

To assess the sample permeabilities at the selected strain levels, flow in the pore space was simulated using resolved finite volume method simulations. These simulations were fully resolved, meaning that the individual pores were discretised. The simulations were carried out using the open-source software OpenFOAM (OpenFOAM 2022, Weller et al. 1998). Within OpenFOAM, the incompressible steady state turbulent solver, SimpleFOAM was used to solve the velocity and pressure fields. SimpleFOAM achieves convergence by following a SIMPLE algorithm (see Greenshields et al. 2022 for details). The complexity of the pore space topology meant that a fine mesh was required. An optimum mesh-element size selection must provide an accurate solution at a reasonable computational cost.

To render the simulations computationally tractable for each of the DEM samples, a segmentation procedure was applied. Original samples were divided into smaller sub-samples to assess the spatial variation and optimise computational performance. Different splitting procedures were tested, and the void ratio and PSD of each sub-sample were calculated. Subsets were considered representative when the void ratio and PSD were equivalent to that of the whole sample.

To generate the sub-samples, the original sample was first reduced by 10% in each direction and then divided into 8 particle subsets. Depending on the strain level, the sub-samples comprised ~1,600-1,700 particles each. Subsets were employed as input to OpenFOAM to simulate permeameter tests in the three orthogonal axes.

An inlet and an outlet were added in the direction of flow. A gap of $1x10^{-4}$m between the particles and the inlet/outlet was included to allow full development of the flow field. No-slip and slip (symmetry) boundary conditions were applied at the particle surface and perpendicular boundary faces, respectively. The slip condition implies that the normal velocity remains zero while the tangential velocity is unconstrained (Zhao & O'Sullivan, 2022). The maximum Reynold's number of all simulations was about 0.2, which is below the Darcy-laminar flow limit, usually identified between 1-10 (Bear, 1988). A summary of all the simulation parameters is indicated in Table 2.

An unstructured tetrahedral mesh, generated through a modified version of the mesh-sphere library (Knight 2022, 2019), was employed to discretize the void space. Mesh quality was validated by reproducing the analytical permeability and drag expressions developed by Zick and Homsy (1982) for monodisperse packages. From these prototype tests, a characteristic length of $5.78x10^{-6}$ m for the sub-sample simulations was found to be an adequate

trade-off between accuracy and computational cost. The average element volume for all simulations was about $1x10^{-16}$ m^3.

Table 2. Permeameter simulation parameters

Parameter	Value	Units
Characteristic length, s_c	$5.78x10^{-6}$	m
Average element size, δv	$1x10^{-16}$	m^3
Fluid density, ρ_f	1000	kg/m^3
Maximum Reynold's number, Re	0.2	-
Inlet velocity, v_i	0.002, 0.004	m/s

Along each orthogonal direction (i.e., x,y,z), two different velocities were tested. Each velocity value was imposed in the inlet as a boundary condition. After convergence, the pressure drop was extracted for each test. From these values, intrinsic permeability was determined by applying a linear fit to Darcy's law. Fig. 4 illustrates the velocity field and boundary conditions for flow applied along the x-axis. The outlet and inlet conditions are shown in green lines. The color scale indicates the velocity magnitude in each element. This subset is comprised of 1,642 particles.

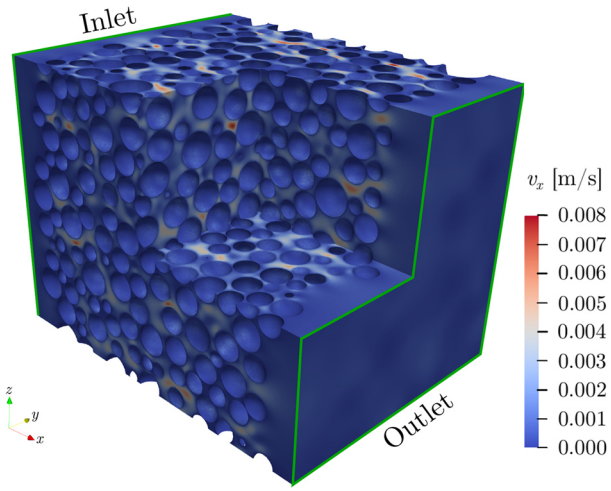

Figure 4. Finite volume simulation. Velocity field magnitude. Flow applied in the x-direction. The sub-sample is comprised of 1,642 particles. Inlet and outlet boundaries are outlined with green lines.

3.2. Permeability Test Results

From the finite-volume simulations, different permeability values were calculated. Fig 5(a) shows the permeability in the three orthogonal directions (i.e., k_{xx}, k_{yy}, k_{zz}) as a function of the vertical strain level, ε_z. Drained and undrained results are represented as continuous and dashed lines, respectively. Fig. 5b displays the permeability ratios k_{xx}/k_{zz} and k_{yy}/k_{zz}). Fig.5c shows the variation in the equivalent or bulk permeability k_{eq}, defined as the square root of the sum of all orthogonal directions. It is important to point out that the results displayed in Fig. 5 correspond to one of the eight split sub-samples.

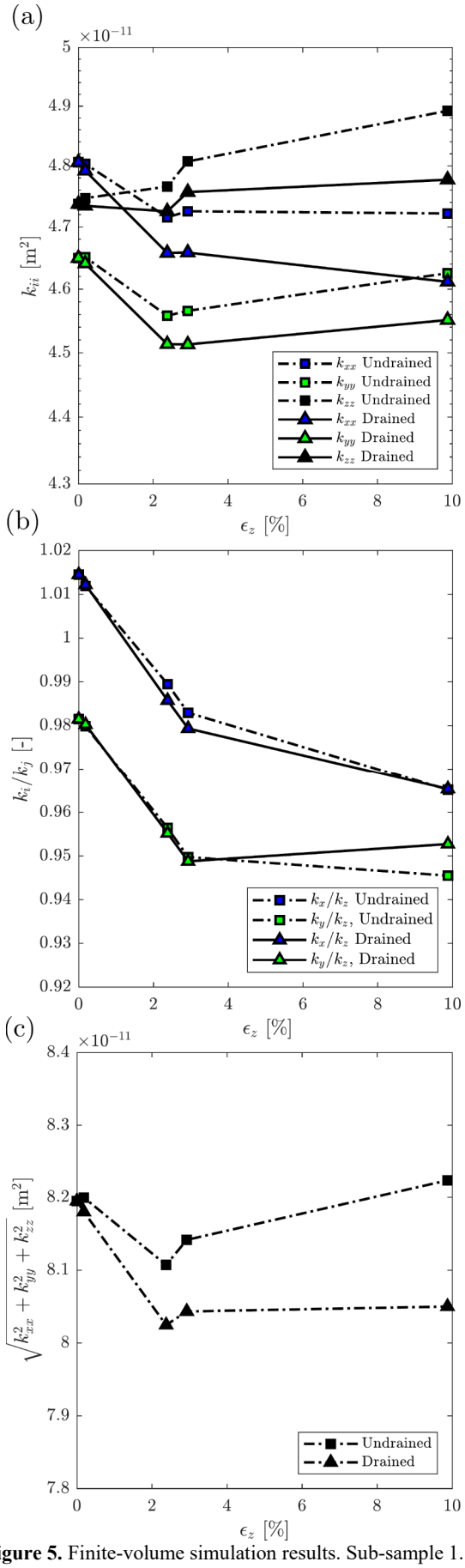

Figure 5. Finite-volume simulation results. Sub-sample 1. (a) axial strain versus intrinsic permeability, (b) axial strain versus permeability ratio, and (c) axial strain versus equivalent permeability.

3.3. Shear-Induced Permeability Changes

Prior to shearing, a 4% difference is observed between the k_{xx} and k_{yy} values. The $\varepsilon_z - k_{ii}$ curves shown in Fig.5a indicate an increase in permeability along the loading direction (z-axis, major principal stress). An opposite trend is observed for the perpendicular direction, where a reduction in permeability takes place as the sample is sheared (x and y-axes, intermediate principal stresses). Similar trends can be observed in both drained and undrained samples. Overall, the intrinsic permeability fluctuates between 1-4% around its isotropic-stress state value (ε_z=0), with larger variations observed in the drained samples.

When comparing different strain levels, it is possible to detect that permeability variations mostly occur for axial strains between 0.2% and 3%. Only subtle changes are observed for subsequent strain levels. In the undrained case, permeability changes coincide with the onset of a fully liquefied state. A major drop in the coordination number takes place between 2.5% and 3% of axial strain, reflecting a loss of contacts. On the other hand, drained variations can be associated with an initial sample contraction, which fades around 3.5% percent. Contraction is suppressed as dilation starts to dominate the overall volumetric behaviour (see Fig. 3(c)) at higher strain levels.

Either drained or undrained, permeability variations can be explained due to pore distortion and fabric changes driven by shearing. As demonstrated by Shire et al. (2013) void elongation with an increase in constriction diameters occurs in voids that are orientated in the direction of the major principal stress and the constrictions narrow in the orthogonal directions. The increase in constriction sizes reduces resistance to flow in the load direction, leading to an increase in permeability. On the other hand, the narrowing of constrictions in the perpendicular direction might obstruct or collapse established flow paths and reduce the overall permeability.

No clear difference between drained and undrained samples is observed for the anisotropy permeability ratio shown in Fig. 5(b). The relation between permeability ratio and strain level could be exclusively controlled by the main principal stress, although, further data is needed to confirm or discard this hypothesis.

The equivalent or bulk permeability results in Fig. 5(c) indicate that, for the strain levels considered, an overall reduction in permeability is only observed for the drained tests. Qualitatively, drained equivalent permeability seems to respond to the volumetric strain of the sample, ε_{vol}. Both, $\varepsilon_z - \varepsilon_{vol}$ (Fig. 3(b)), and $\varepsilon_z - k_{eq}$ curves exhibit a similar shape. A volumetric strain ε_{vol} of 0.15% is attained for a 10% of axial strain ε_z.

The Kozeny-Carman equation (KC) (Carman 1956, Kozeny 1927) is a well-established approach to estimate permeability in porous media. It establishes that permeability changes can only take place when porosity ϵ or volumetric changes occur. The relation between porosity and pressure drop is exponential and its magnitude depends on a series of parameters that that account for particle shape, diameter, and tortuosity. From the generalised form of the KC and Darcy's law, intrinsic permeability k can be expressed as,

$$k = \left(\frac{\emptyset_s{}^2 d_p{}^2}{T_m}\right)\frac{\epsilon^3}{(1-\epsilon)^2} \quad (1)$$

where $\emptyset_s$, d_p and T_m are sphericity, average diameter, and an empirical constant that represents tortuosity and packed bed characteristics.

If KC is assumed to be valid for shearing, permeability changes cannot exist under undrained conditions. However, a commonly overlooked assumption of KC is that the ratio between sample length and average flow-path length remains fixed, which implies a constant tortuosity. Metrics in this assumption only involve the main flow direction (1D), so distortions such as pore elongation cannot be accounted for. Furthermore, evidence provided by Shire et al. (2013) showed that constriction orientation changes during triaxial compression, which could change the average flow-path length. Data published by Morimoto et al. (2022) indicates that the shape of the local void space and the conductance between pores control the overall permeability in polydisperse spherical assemblies. All these features suggest that a variable tortuosity needs to be considered to predict permeability changes under shearing.

Based on the simulation results, and inferring how their pore space evolves with shearing (Shire et al. 2013), it can be hypothesised that permeability variations Δk are driven by two combined effects: pores distortion and volumetric changes. Mathematically, this can be synthesised as,

$$\Delta k = \Delta k_{T_c}(\varepsilon_z) + \Delta k_v(\varepsilon_{vol}) \quad (2)$$

were Δk_{T_c} and Δk_v are the contribution of tortuosity and volumetric changes. Under undrained loading, only the tortuosity term exists, whereas in the drained case, both effects coexist. Comparison between both drained and undrained simulations suggests that the volumetric term dominates drained triaxial shearing. Still, permeability changes in for drained and undrained tests are small, and within the same order of magnitude for the range of axial strains tested (up to 10%). Additional data is required to confirm or discard this hypothesis for further strain levels and different loading paths.

4. Conclusions

The influence of shearing on the permeability of loose-to-medium sands was investigated for monotonic undrained and drained triaxial conditions. DEM and finite-volume simulations were undertaken to estimate intrinsic permeability in the three orthogonal directions at characteristic strain levels. From the simulation results, it can be concluded:

- Triaxial shear deformation induces permeability anisotropy in drained and undrained triaxial conditions. In both cases, the anisotropy increases with increasing axial strain. An increase in permeability is induced along the major principal stress direction, whereas a reduction is observed in

the intermediate principal stress direction. Trends are consistent with the results published by Kuhn et al. (2015) for drained biaxial compression under plain strain conditions.

- For the strain levels analysed in this article, shear-induced permeability changes are about 1-4% depending on the flow direction. Conventional testing methods are not suitable to measure these changes due to their magnitude and directionality.
- Undrained simulation results indicate that a sudden increase in vertical permeability around the onset of liquefaction, which can be attributed to a sudden loss of particle contacts, and a re-distribution of the void space. These findings are consistent with hypotheses proposed by other authors for cyclic loading.
- Results show that permeability changes can take place even in absence of porosity changes. Conceptually, changes in shearing can be attributed to pore distortion and volumetric strains in the sample. Pore distortion is the driving mechanism that induces undrained permeability changes, whereas for drained loading, both pore distortion and volumetric strains contribute to permeability changes.

Acknowledgements

The authors are grateful for the financial support provided by ANID-Chile (grant #: 72210108). All LAMMPS and OpenFOAM simulations were performed on the Imperial College Research Computing System facilities. (doi: 10.14469/hpc/2232).

References

Adamidis, O., and G. S. P. Madabhushi. 2018. "Partial drainage during earthquake-induced liquefaction." In Physical Modelling in Geotechnics, pp. 937-942. CRC Press. https://doi.org/10.1201/9780429438646-26

ASTM. 2016. “Standard Test Methods for Measurement of Hydraulic Conductivity of Saturated Porous Materials Using a Flexible Wall Permeameter”. ASTM D5084, Annual Book of Standards, ASTM International, West Conshohocken, PA.

Bayoumi, A., A. Mhenni, M. Chekired, and M. Karray. 2022. "Porous Stones in Permeability Measurement: Drawbacks and Solution." Canadian Geotechnical Journal. https://doi.org/10.1139/cgj-2021-0400

Bear, J. 1988. “Dynamics of fluids in porous media”. Courier Corporation.

Bray, J. D., and D. Hutabarat. 2022. "CPT-based liquefaction ejecta evaluation procedure." In Cone Penetration Testing 2022, pp. 844-849. CRC Press. https://doi.org/10.1201/9781003308829-125

Carman, P. C. 1956. "Flow of gases through porous media".

Chapuis, R. P. 2012. "Predicting the saturated hydraulic conductivity of soils: a review." Bulletin of engineering geology and the environment 71, no.3, pp. 401-434. https://doi.org/10.1007/s10064-012-0418-7

Daniel, D.E., D.C., Anderson, S.S., Boynton. 1985. “Fixed-Wall Versus Flexible-Wall Permeameters”. Hydraul. Barriers Soil Rock. https://doi.org/10.1520/STP34573S

Dinesh, N., B., Subhadeep, and R., Karpurapu. 2022. "Performance evaluation of PM4Sand model for simulation of the liquefaction remedial measures for embankment." Soil Dynamics and Earthquake Engineering, no. 152. https://doi.org/10.1016/j.soildyn.2021.107042

Duncan, J. M. 2000. "Factors of safety and reliability in geotechnical engineering." Journal of Geotechnical Engineering 126, no. 4. pp. 307-316. https://doi.org/10.1061/(ASCE)1090-0241(2000)126:4(307)

Elgamal, A., E., Parra, Z., Yang, and A., Korhan. 2002. "Numerical analysis of embankment foundation liquefaction countermeasures." Journal of Earthquake Engineering 6, no. 04. https://doi.org/10.1080/13632460209350425

Fioravante, V., D. Giretti, S. Airoldi, and J. Moglie. 2021. "Effects of seismic input, fine crust and existing structure on liquefaction from centrifuge model tests." Bulletin of Earthquake Engineering 19, no. 10 , pp. 3807-3833. https://doi.org/10.1007/s10518-021-01139-4

Greenshields, C., and H. Weller. 2022."Notes on Computational Fluid Dynamics: General Principles." CFD Direct Ltd.: Reading, UK.

Haigh, S. K., J. Eadington, and S. P. G. Madabhushi. 2012. "Permeability and stiffness of sands at very low effective stresses." Géotechnique 62, no. 1, pp. 69-75. https://doi.org/10.1680/geot.10.P.035

Huang, X., K. J. Hanley, C. O'Sullivan, and F. CY Kwok. 2014. "Effect of sample size on the response of DEM samples with a realistic grading." Particuology 15, pp. 107-115. https://doi.org/10.1016/j.partic.2013.07.006

Hutabarat, D., and J.D, Bray. 2021. "Effective stress analysis of liquefiable sites to estimate the severity of sediment ejecta" Journal of Geotechnical and Geoenvironmental Engineering 147, no. 5. https://doi.org/10.1061/(ASCE)GT.1943-5606.0002503

Knight C., 2019. “Fluid flow and drag in polydisperse granular materials subject to laminar seepage flow”. Ph.D. thesis, Imperial College London, London, UK. https://doi.org/10.25560/67823.

Knight, C.. 2021. mesh-sphere-packing. https://github.com/chrisk314/mesh-sphere-packing

Kozeny, J.. 1927. "Uber kapillare leitung der wasser in boden." *Royal Academy of Science, Vienna, Proc. Class I* 136, pp. 271-306.

Kuhn, M. R., W. Sun, and Q. Wang. 2015. "Stress-induced anisotropy in granular materials: fabric, stiffness, and permeability." Acta Geotechnica 10, no. 4, pp. 399-419. https://doi.org/10.1007/s11440-015-0397-5

Li, Y., M. Chen Ong, and T. Tang. 2018. "Numerical analysis of wave-induced poro-elastic seabed response around a hexagonal gravity-based offshore foundation." Coastal Engineering 136 , pp. 81-95. https://doi.org/10.1016/j.coastaleng.2018.02.005

Malekmakan, M., H. Shahir, and P. Ayoubi. 2021. "Investigation of liquefaction-induced lateral spreading of gently sloping grounds using a variable permeability model." International Journal for Numerical and Analytical Methods in Geomechanics 45, no. 12, pp. 1809-1832. https://doi.org/10.1002/nag.3243

OpenFOAM. .Accessed April 20, 2022. https://www.openfoam.com/

OpenFOAM Foundation, OpenFOAM v7 User Guide, https://cfd.direct/openfoam/

Plimpton, S.. 1995. "Fast parallel algorithms for short-range molecular dynamics." Journal of computational physics 117, no. 1, pp.1-19. https://doi.org/10.1006/jcph.1995.1039

Potts, D.M., L., Zdravković, T., Addenbrooke, K. G., Higgins, and N., Kovačević. 2001. “Finite element analysis in geotechnical engineering: application”. Vol. 2. London: Thomas Telford. https://doi.org/10.1680/feaigea.27831

Robertson, P. K. 2010. "Estimating in-situ soil permeability from CPT & CPTu." In Memorias del 2nd International Symposium on Cone Penetration Testing, California State Polytechnic University Pomona, CA.

Shahir, H., B. Mohammadi-Haji, and A. Ghassemi. 2014. "Employing a variable permeability model in numerical simulation of saturated sand behavior under earthquake loading." Computers and Geotechnics 55, pp.211-223. https://doi.org/10.1016/j.compgeo.2013.09.007

Shaker, A. A., M. Dafalla, A. M. Al-Mahbashi, and M. A. Al-Shamrani. 2022. "Predicting Hydraulic Conductivity for Flexible Wall Conditions Using Rigid Wall Permeameter." Water 14, no. 3 pp.286-292. https://doi.org/10.3390/w14030286

Shire, T., C. O'Sullivan, D. Barreto, and G. Gaudray. 2013. "Quantifying stress-induced anisotropy using inter-void constrictions." *Géotechnique* 63, no. 1, pp 85-91. https://doi.org/10.1680/geot.11.T.020

Verdugo, R., and K. Ishihara. 1996. "The steady state of sandy soils." Soils and foundations 36, no. 2, pp-81-91. https://doi.org/10.3208/sandf.36.2_81

Wang, L. 2021. "Vertical response of a pile embedded in highly-saturated soil with compressible pore fluid and anisotropic permeability." Computers and Geotechnics no. 140. https://doi.org/10.1016/j.compgeo.2021.104462

Weller H. G., G. Tabor, H. Jasak, C. Fureby. 1998. "A tensorial approach to computational continuum mechanics using object-oriented techniques", Computers in Physics, vol. 12, no. 6. https://doi.org/10.1063/1.168744

Xie, X., B. Ye, T. Zhao, X. Feng, and F. Zhang. 2021. "Changes in sand mesostructure under repeated seismic liquefaction events during centrifuge tests." Soil Dynamics and Earthquake Engineering no. 150,. https://doi.org/10.1016/j.soildyn.2021.106940

Yang, J. and H. Y., Sze. 2011. "Cyclic behaviour and resistance of saturated sand under non-symmetrical loading conditions". Géotechnique 61, no.1, pp. 59–73. https://doi.org/10.1680/geot.9.P.019

Zhao, B., and C. O'Sullivan. 2022. "Fluid particle interaction in packings of monodisperse angular particles." Powder Technology no. 395, pp. 133-148. https://doi.org/10.1016/j.powtec.2021.09.022

Zick, A. A., and G. M. Homsy. 1982. "Stokes flow through periodic arrays of spheres." Journal of fluid mechanics no. 115, pp. 13-26. https://doi.org/10.1017/S0022112082000627